APL Materials

Highly charged interface trap states in PbS_{1-x} govern electro-thermal transport

Cite as: APL Mater. **7**, 071105 (2019); https://doi.org/10.1063/1.5096786
Submitted: 19 March 2019 . Accepted: 13 June 2019 . Published Online: 16 July 2019

Sajad Yazdani, Tran Doan Huan, Yufei Liu, Raana Kashfi-Sadabad, Raul David Montaño, Jian He, and Michael Thompson Pettes

Highly charged interface trap states in PbS_{1-x} govern electro-thermal transport

Cite as: APL Mater. 7, 071105 (2019); doi: 10.1063/1.5096786
Submitted: 19 March 2019 • Accepted: 13 June 2019 •
Published Online: 16 July 2019

Sajad Yazdani,[1,2] Tran Doan Huan,[2,3] Yufei Liu,[4] Raana Kashfi-Sadabad,[2] Raul David Montaño,[1,5] Jian He,[4] and Michael Thompson Pettes[1,2,6,a)]

AFFILIATIONS

[1]Department of Mechanical Engineering, University of Connecticut, Storrs, Connecticut 06269, USA
[2]Institute of Materials Science, University of Connecticut, Storrs, Connecticut 06269, USA
[3]School of Materials Science and Engineering, Georgia Institute of Technology, Atlanta, Georgia 30332, USA
[4]Department of Physics and Astronomy, Clemson University, Clemson, South Carolina 29634, USA
[5]Department of Aerospace and Mechanical Engineering, University of Arizona, Tucson, Arizona 85721, USA
[6]Center for Integrated Nanotechnologies, Materials Physics and Applications Division, Los Alamos National Laboratory, Los Alamos, New Mexico 87545, USA

[a)]**Author to whom correspondence should be addressed:** pettesmt@lanl.gov

ABSTRACT

This work describes our discovery of the dominant role of highly charged interfaces on the electrothermal transport properties of PbS, along with a method to reduce the barrier potential for charge carriers by an order of magnitude. High temperature thermoelectrics such as PbS are inevitably exposed to elevated temperatures during postsynthesis treatment as well as operation. However, we observed that as the material was heated, large concentrations of sulfur vacancy ($V_{\ddot{S}}$) sites were formed at temperatures as low as 266 °C. This loss of sulfur doped the PbS *n*-type and increased the carrier concentration, where these excess electrons were trapped and immobilized at interfacial defect sites in polycrystalline PbS with an abundance of grain boundaries. Sulfur deficient $PbS_{0.81}$ exhibited a large barrier potential for charge carriers of 0.352 eV, whereas annealing the material under a sulfur-rich environment prevented $V_{\ddot{S}}$ formation and lowered the barrier by an order of magnitude to 0.046 eV. Through *ab initio* calculations, the formation of $V_{\ddot{S}}$ was found to be more favorable on the surface compared to the bulk of the material with a 1.72 times lower formation energy barrier. These observations underline the importance of controlling interface-vacancy effects in the preparation of bulk materials comprised of nanoscale constituents.

Lead sulfide is a well-known thermoelectric material that has attracted attention due to the environmental abundance of sulfur.[1,2] Compared to the Pb–Se and Pb–Te, the Pb–S bond is stronger which makes PbS a more stable material.[1,3] PbS has a larger room temperature band gap (0.41 eV) than those of PbSe (0.29 eV) and PbTe (0.32 eV);[4] thus, the maximum zT can be obtained at a higher temperature.[5] This makes PbS favorable for high-temperature applications[6,7] considering its high melting temperature of 1391 K.[8] However, the lattice thermal conductivity of bulk PbS (2.50 W m^{-1} K^{-1} at room temperature) has been found to be higher than those of PbTe (1.99 W m^{-1} K^{-1}) and PbSe (1.62 W m^{-1} K^{-1}).[9] This large lattice thermal conductivity has hindered the effective use of PbS for thermoelectric applications. Alloying,[10] nanoscale precipitations,[3,11] and bottom-up synthesis of nanostructures[6,12,13] have been utilized in order to reduce the thermal conductivity of PbS-based material systems. Generally, having a high density of grain boundaries of the appropriate sizes is appealing for thermoelectric applications as the lattice thermal conductivity can adequately be suppressed by scattering the majority of heat-carrying phonons. First principles calculations of thermal conductivity accumulation have predicted that nanostructures of ~10 nm can be used to effectively reduce the room-temperature thermal conductivity for PbSe, PbTe, SnS, and SnSe by as much as 80%–90%.[14–16] The advancements in solution-processed syntheses of nanocrystals have made achieving such size

ranges quite feasible.[17] However, it is often reported that chemistry-processed materials exhibit much lower electrical conductivities when compared to conventional top-down (solid-state) materials due to the presence of point defects and remaining organic residues introduced during the synthesis. In order to remove the insulating ligands and organic species, most of these materials are annealed at high temperatures (above 400 °C) under vacuum or an inert gas environment.[12,13,18,19] This exposure to high temperatures can promote vacancy site formations. Sulfur losses have been reported to take place, both during material preparations[20,21] and during operations at high temperatures (above 400 °C).[7,22] The presence of point defects and interfaces can significantly alter the electronic properties of materials and dominate both the Seebeck coefficient and electrical conductivity. For example, while bulk Bi_2Te_3 is known to be *p*-type for the stoichiometric and Bi-rich cases, Mehta *et al.*[20] reported a majority carrier reversal in solution-processed Bi_2Te_3 pellets showing *n*-type behavior due to the presence of point defects. This majority carrier type reversal has also been observed through changes in the surface condition of $(Bi_{1-x}Sb_x)_2Te_3$ nanoplates.[23] Point defects may also interact with dopants present in a thermoelectric material;[24] however, the dopant–defect interactions have not been fully understood. The abundance of grain boundaries and interfaces in solution-processed materials or mechanically processed nanomaterials[25] can make these interactions even more complicated. The structure of grain boundaries consisting of layers of disordered atoms is complex. These atomic layers can be considered as transitions between various orientations of crystallites with a high defect concentration.[26] It has been suggested that these interfacial defects can act as trapping states by immobilizing charge carriers.[26–28] Therefore, the number of available carriers for conduction decreases and the mobile carrier concentration can be much lower than the doping concentration.[26] In addition, the trapped-carriers cause the grain boundaries to be electrically charged, as has been reported for PbS[25,29,30] and PbTe.[31,32] These charged interfaces can act as potential barriers, obstructing the charge transfer and decreasing the mobility.[26] The charged layer is balanced by two layers of opposite charges on both sides of the interface[27] which results in the formation of a dipole layer with a width correlated with the strength of the potential barrier.[33] Fully understanding these interfacial defects is highly relevant to end-use performance since for waste-heat recovery applications, it is more preferable to operate at elevated temperatures from a thermodynamic stand point.[6]

This work investigates sulfur vacancy formation ($V_{\ddot{S}}$) and its effect on the thermoelectric properties of solution-processed PbS. Although the abundance of grain boundaries in bottom-up materials is favorable for thermal conductivity reduction, defective interfaces can be charged by $V_{\ddot{S}}$ and impede electrical transport. The sulfur concentration is measured after each synthesis and postsynthesis step in order to track the stage at which sulfur loss occurs. Through a theoretical investigation, the tendency of $V_{\ddot{S}}$ formation is evaluated both from the surface and from the bulk of the material. In addition, the feasibility of the sulfur-loss prevention by annealing under a sulfur-rich environment is assessed.

Solvothermal reaction, high temperature annealing (600 °C), and spark plasma sintering (SPS) were used for the material preparation. High-temperature annealing can potentially enhance vacancy and defect density, and SPS is essential in order to sinter the grain boundaries and obtain high density solid materials needed for thermoelectric energy conversion. Figure 1 illustrates the synthesis procedure. Thiourea and lead (II) acetate trihydrate were used as the sulfur and lead precursors, and glycerol was used as the solvent. The solvothermal reaction occurred in a Teflon lined autoclave reactor. The obtained sample, denoted as PbS-Solvo, was annealed under H_2/Ar at 600 °C.

Other samples were prepared by annealing the materials under a sulfur-rich environment. During the annealing, a constant flow of sulfur was provided by evaporating the sulfur powder at 150 °C placed in an alumina boat located at the upstream of the PbS-Solvo sample under an H_2/Ar carrier gas. The sulfurized samples were denoted as PbS–S and PbS–S–SPS, referring to the obtained products after sulfurization and after both sulfurization and SPS, respectively. For comparison, the annealing and SPS steps were also conducted on a reference sample made using Sigma-Aldrich PbS (#372595) with a different morphology denoted as PbS-ref.–SPS. After SPS and polishing, the obtained pellets were used for laser flash thermal diffusivity measurements. For the electrical and Seebeck coefficient measurements, rectangular bars were cut from the same pellet used for diffusivity measurements to ensure that the

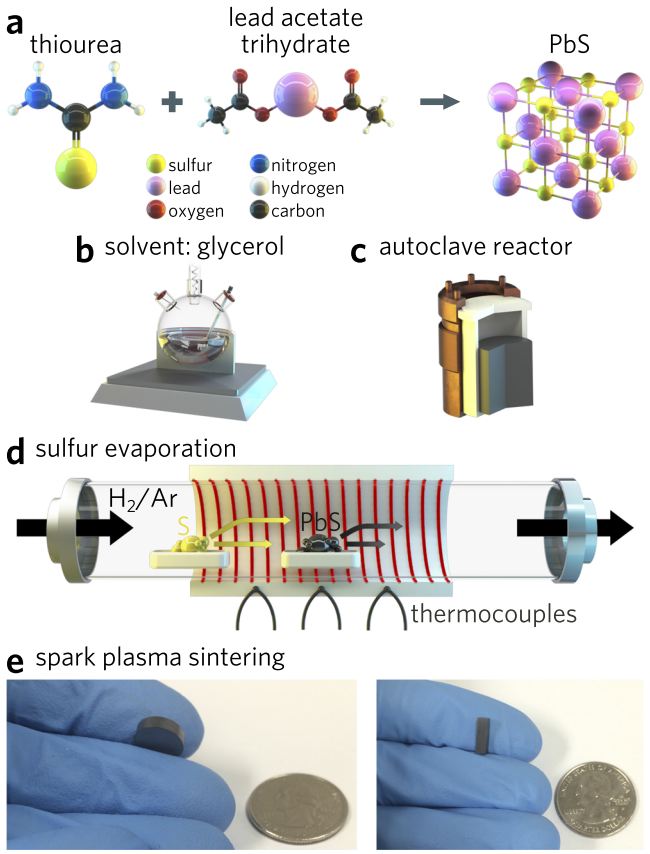

FIG. 1. Illustration of PbS synthesis steps: (a) reaction scheme, (b) and (c) solvothermal autoclave reactions, and (d) sulfur annealing process under H_2/Ar. (e) Representative densified pellet and rectangular bar obtained after spark plasma sintering (SPS) and used in electrothermal measurements.

doping concentration was maintained. The details of the sample treatments are listed in Table I. The synthesis steps and treatments were designed in order to answer the following questions: (i) at which synthesis step of solvothermal reaction, high-temperature annealing, or SPS, are $V_{\ddot{S}}$ sites formed, (ii) can the sulfurization process prevent formation of $V_{\ddot{S}}$, (iii) how does the presence of interfaces affect electrothermal transport properties in samples with and without $V_{\ddot{S}}$, and (iv) how does a different microstructure morphology and grain boundary concentration affect the electrothermal transport properties.

Figure 2 gives the transmission electron microscopy (TEM), scanning TEM (STEM), scanning electron microscopy (SEM), and energy dispersive x-ray spectroscopy (EDS) analysis of the PbS samples after each synthesis step. The sample after the high-temperature Ar annealing (PbS) exhibited a dendrite morphology with high concentrations of grain boundaries, as shown in Figs. 2(a) and 2(c). Figures 2(b) and 2(d) show that the dendrite morphology was preserved after the sulfur treatment as can be seen from TEM and SEM images for PbS–S. Sintering of the grain boundaries and densification for both samples can be observed from the SEM images after SPS in Figs. 2(e) and 2(f). All samples demonstrated a uniform dispersion of Pb and S elements according to EDS analysis.

X-ray diffraction (XRD) patterns of all samples were assigned to the cubic phase of PbS, as shown in Fig. 3(a) and Table S1, supplementary material. The reference sample, PbS-ref.–SPS, showed a larger Scherrer crystallite size of 310 nm compared to those for PbS-SPS (199 nm) and PbS–S–SPS (206 nm). Thermogravimetric analysis (TGA) of the solvothermal product in Fig. 3(b) indicated three major weight loss peaks. The goal of the performed TGA analysis was to identify a temperature range at which any possible S-loss occurred and where $V_{\ddot{S}}$ vacancy sites were formed. The first peak at 166 °C was attributed to the removal of chemisorbed water and solvents. The peak at 244 °C was assigned to the removal of the remaining glycerol [see Fig. 3(d) for the TGA analysis of glycerol]. Assuming that the third peak at 266 °C with a weight loss of 1.97% is due to the sulfur loss from the sample, a vacancy degree of $x = 0.17$ is obtained based on PbS_{1-x}. This calculation was based on a mass-balance equation assuming that the initial sample was stoichiometric according to Ref. 34,

$$M_w(\mathrm{PbS}) = [1 + (\%\ mass\ loss\ in\ \mathrm{N_2})/100] \times M_w(\mathrm{PbS_{1-x}}). \quad (1)$$

This assumption is subsequently verified by inductively coupled plasma optical emission spectroscopy (ICP-OES) analysis. After this major weight loss at 266 °C, only 0.3% weight loss is obtained over the remaining temperature range up to 600 °C. Figure 3(c) shows the differential scanning calorimetry (DSC) shift of the endothermic peak from 971 to 1053 °C after SPS, being an indication of grain boundary sintering by SPS.

ICP-OES analysis of the solvothermally synthesized sample (PbS-Solvo) revealed that the atomic ratio of S was only 0.46% higher than that of the Pb which indicated that the product of the solvothermal process did not have sulfur deficiency. Having a near stoichiometric as-synthesized sample verified our prior assumption for the calculation of x based on TGA. Interestingly, the H_2/Ar annealing at 600 °C induced a substoichiometric PbS_{1-x} sample with $x = 0.16$. This value is very close to the value obtained from TGA analysis ($x = 0.17$), indicating that the sulfur loss temperature range was

TABLE I. Sample descriptions, inductively coupled plasma optical emission spectrometry (ICP-OES) analysis results, sulfur under-stoichiometry degree, estimated lower and upper limits of carrier concentrations and the densities of trap states, and barrier height for charge carriers during transport.

Sample	Sample description	Measured ICP-OES (atom %)		Estimated carrier concentration at 300 K					
		Pb	S	x in PbS_{1-x}	Mobile carriers n/p (cm^{-3})	Trap state density Q_t (cm^{-2})	N_{ICP}/P_{ICP} (cm^{-3})	Trap state density Q_t (cm^{-2})	Barrier height (eV)
PbS-solvo	After the solvothermal reaction	49.77	50.23	−0.01	...	...	...	...	...
PbS	After argon annealing at 600 °C	54.38	45.62	0.16	...	...	...	...	...
PbS-SPS	After SPS at 600 °C	55.40	44.6	0.19	3.72×10^{19}	1.44×10^{13}	7.40×10^{21}	2.04×10^{14}	0.352
PbS–S	After sulfur treatment at 600 °C	48.51	51.49	−0.06	...	...	...	...	...
PbS–S–SPS	After SPS at 600 °C	49.18	50.82	−0.03	1.8×10^{18}	1.16×10^{12}	1.17×10^{21}	2.92×10^{13}	0.046
PbS-ref.–SPS (Sigma-Aldrich #372595)	After SPS at 600 °C	50.98	49.02	0.04	1.7×10^{18}	2.02×10^{12}	1.56×10^{21}	6.12×10^{13}	0.151

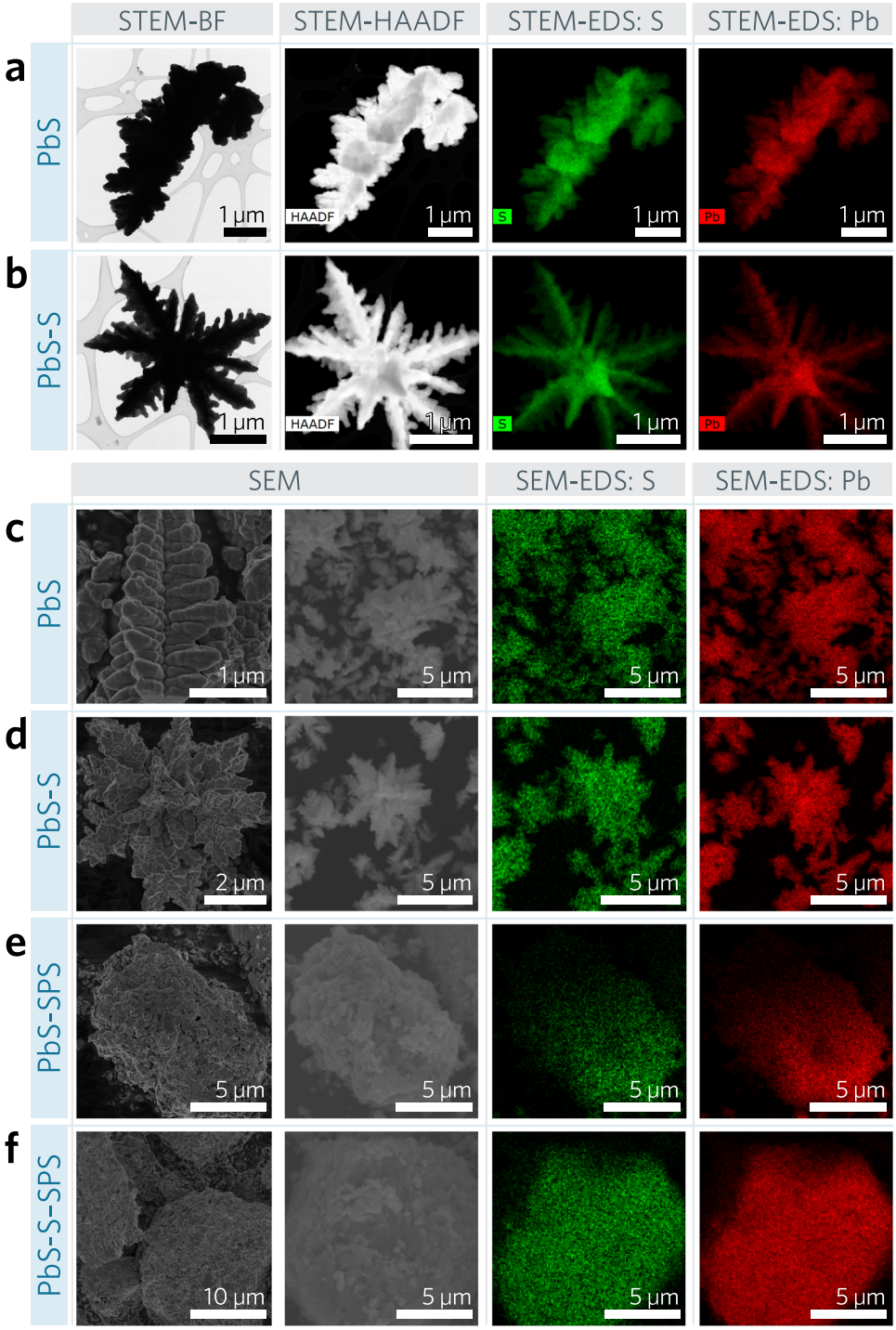

FIG. 2. TEM and HAADF-STEM images of the PbS_{1-x} samples: (a) after the H_2/Ar treatment (PbS) and (b) after sulfur treatment (PbS–S). SEM and EDS images for (c) PbS and (d) PbS–S are shown for comparison. SEM and EDS images of the PbS_{1-x} samples after SPS: (e) PbS-SPS and (f) PbS–S–SPS. The elemental mappings are based on the sulfur K series and lead M series.

identified properly. The SPS process at 600 °C further increased the substoichiometry parameter to $x = 0.19$ (sample PbS-SPS). Analysis of the sulfur treated sample, PbS–S, showed that the postsynthesis sulfurization indeed prevented sulfur deficiencies in the sample. A value of $x = -0.06$ was obtained for PbS–S, in which the negative sign indicated the presence of excess sulfur. During SPS, some of the excess sulfur was evaporated and $x = -0.03$ was obtained for PbS–S–SPS. The reference sample (PbS-ref.–SPS.) was found to be slightly

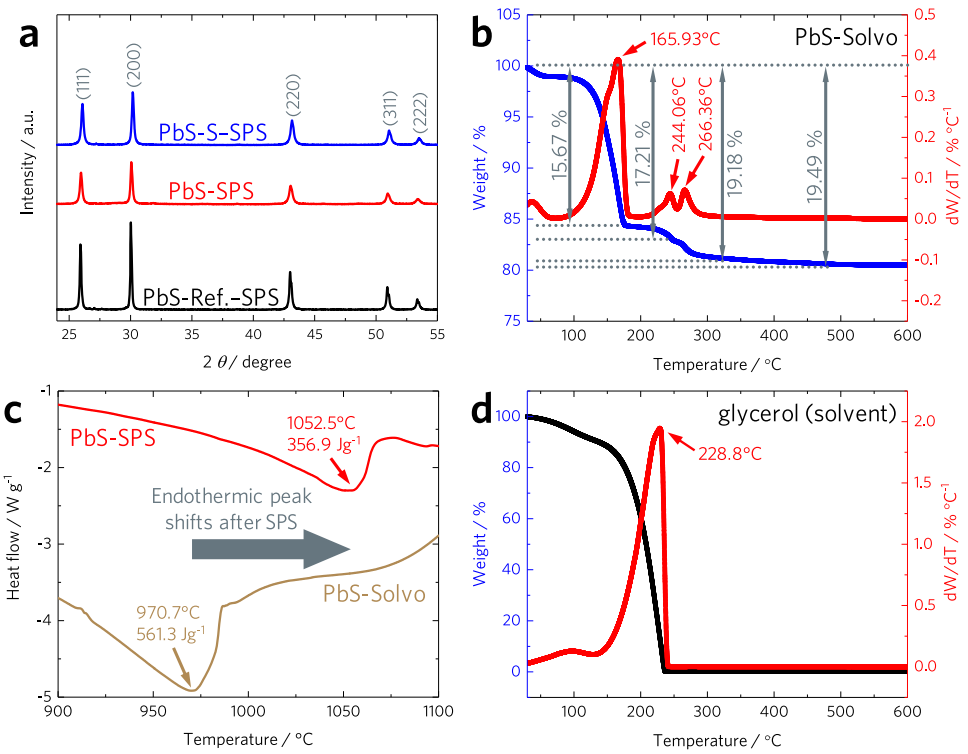

FIG. 3. (a) X-ray diffraction patterns of PbS samples after spark plasma sintering (SPS) at 600 °C. The peaks are assigned to the cubic PbS phase with space group Fm3m(225) according to powder diffraction file #05–0592. (b) TGA analysis of the solvothermal product. (c) DSC analysis of the samples before and after SPS. (d) TGA analysis of glycerol, identifying the glycerol removal temperature range.

substoichiometric after SPS at 600 °C, with $x = 0.04$. A summary is given in Table I.

The performed TGA and ICP-OES analyses revealed several important observations: (i) sulfur loss occurred during the high-temperature annealing and not during the solvothermal process, (ii) the sulfur-loss peak was centered at 266 °C, and (iii) high temperature annealing (600 °C) in the presence of sulfur vapor prevented sulfur loss from the PbS. In order to gain deeper insight, density functional theory (DFT) calculations of $V_{\ddot{S}}$ formation energy were performed on the surface as well as the bulk of the materials (Fig. S1, supplementary material). The PbS crystal with no vacancy was taken as the reference. Then, one sulfur atom was removed from either the surface or the bulk. The removal process was modeled both thermodynamically and kinetically using the nudged elastic band method coupled with DFT calculations. Our calculated transition pathways are given in the supplementary material, showing that removing a surface sulfur atom is far easier than removing a bulk (or deeper-layer) sulfur atom, which needs to overcome a barrier of more than 8 eV, about 1.7 times larger than the former case (see Fig. S1, supplementary material). This can explain the sulfur loss being a major event at 266 °C due to sulfur evaporations from layers closer to the outer surfaces, which is observable due to the dendritic morphology of PbS-Solvo.

Temperature-dependent electrical conductivity of the samples is shown in Fig. 4(a). The electrical conductivity of PbS-SPS with $x = 0.19$ (the sample with the highest concentration of $V_{\ddot{S}}$) exhibited a small decrease from 20.6 to 14.3 S cm^{-1} as the temperature increased from 29 to 144 °C. From 191 to 337 °C, the electrical conductivity showed a rapid increase to 71.7 S cm^{-1}. Above this range, the electrical conductivity remains fairly constant. Such behavior can be caused by solid-state chemical reactions upon cycling as has been reported previously.[29] However, TGA analysis did not suggest the possibility of any reaction in the samples annealed and spark plasma sintered at 600 °C. The other reason for such a trend in the electrical conductivity can be due to a change in the majority carrier type due to increasing carrier concentration by thermal activation.[19] In such cases, a concurrent sign inversion in the measured Seebeck coefficient is expected. However, the PbS-SPS sample demonstrates an *n*-type behavior over the entire temperature range with no sign inversion, as shown in Fig. 4(b). Another explanation can be due to existence of potential barriers in the sample. As the temperature increases above ~450 K, some of the charge carriers gain enough energy to overcome the barrier caused by charged grain boundaries according to the model proposed by Seto.[26] The sulfurized sample, PbS–S–SPS with $x = -0.03$, exhibited a steady increase in the electrical conductivity as temperature increased, as shown in Fig. 4(a). A maximum value of 14.4 S cm^{-1} was measured at 582 °C. Interestingly, the Seebeck coefficient measurements showed *p*-type behavior over the entire temperature range with a maximum of $S = 373\ \mu V\ K^{-1}$ at a temperature of 192 °C. The *p*-type behavior suggests the existence of excess sulfur with no $V_{\ddot{S}}$, which is consistent with the ICP-OES analysis. Additionally, although the sulfur vacancy formation was theoretically modeled with the assumption that the sulfur atom was completely removed from the sample (and therefore no interstitial sulfur formation), it is possible that there were sulfur atoms trapped by the complicated energy landscape, therefore making an additional contribution to the *p*-type behavior of the measured Seebeck coefficient.

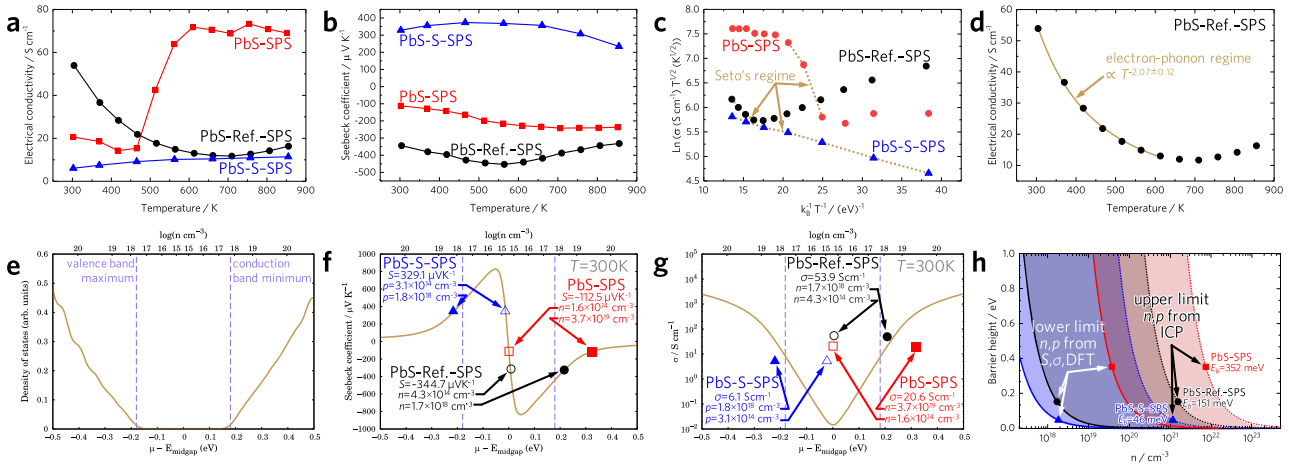

FIG. 4. Temperature dependent (a) electrical conductivity and (b) Seebeck coefficient measurements of the PbS samples. (c) Logarithm of electrical conductivity times square root of temperature vs $(k_B T)^{-1}$ allows for calculation of the barrier heights according to Seto's model.[26] (d) Modeling of the electrical conductivity of PbS-ref.–SPS sample based on electron-phonon dominant scattering. (e) DFT calculation of PbS electronic density of states. (f) Seebeck coefficient calculated by DFT/BoltzTraP vs relative chemical potential. Carrier concentrations can be estimated from comparison with room temperature experimental values. Degenerate regime carrier concentrations are indicated by solid symbols, and the values closer to the intrinsic regime are shown by open symbols. (g) Electrical conductivity, σ, calculated by DFT/BoltzTraP vs relative chemical potential shown in comparison with experimental values plotted at carrier concentrations obtained in (f). The sample chemical potentials are clearly not in the intrinsic regime. (h) Calculated barrier height vs carrier concentrations. The estimated carrier concentration values based on DFT were considered as the lower limit (solid lines), and the carrier concentrations obtained based on the ICP-OES analysis were considered as the upper limit (dotted lines).

The linear region of the curves of $\ln(\sigma T^{1/2})$ vs $1/(k_B T)$ in Fig. 4(c) was taken in order to estimate the barrier heights for charge carriers during transport based on the following expression:[26]

$$\sigma \propto T^{-1/2} \exp\left(-E_B / K_B T\right) \text{ for } NL > Q_t, \quad (2)$$

where T, k_B, E_B, N, L, and Q_t are the temperature, Boltzmann constant, barrier height, doping concentration, crystallite size, and trap state density, respectively.

Figure 4(d) illustrates that in contrast to PbS-SPS and PbS–S–SPS, the reference sample (PbS-ref.–SPS) shows a trend that is expected for degenerate/metallic electrical conduction dominated by electron-phonon scattering where below ~325 °C, the electrical conductivity is proportional to T^n with $n = -2.07 \pm 0.12$. This is slightly higher than the expected value of $n = -3/2$, possibly due to additional scattering mechanisms in the sample. However, at temperatures above 325 °C, the behavior changes, and the electrical conductivity is seen to increase from 12 to 16.3 S cm^{-1} at 388–612 °C, respectively. The different trend and values of the temperature dependent electrical conductivity of the PbS-SPS and PbS-ref.–SPS samples are attributed to the different grain boundary concentrations and the corresponding energy barriers introduced by the charged-grain boundaries. The distinct morphology of the original powders induced different grain boundary concentrations during the SPS although both samples were treated at the same temperature of 600 °C. The density of the PbS-ref.-SPS sample (7.34 g cm^{-1}) was measured to be close to the theoretical value (7.6 g cm^{-1}) and higher than that of the PbS-SPS (6.28 g cm^{-1}). In addition, the x value of the PbS-ref.–SPS was found to be lower than that of the PbS-SPS (0.04 compared to 0.19, as shown in Table I) which can also contribute to the distinct temperature dependent electrical conductivities of these samples. Figure 4(b) shows that the Seebeck coefficient of the reference sample exhibits an n-type behavior with a maximum $S = -453.5$ μV K^{-1} at $T = 291$ °C.

According to the trap state model given by Eq. (2),[26] the doping concentration N can be larger than the mobile carrier concentration n as a portion of the carriers is immobilized in the trap states at interfaces. In the current work, n is estimated by a comparison between the measured Seebeck coefficients and those obtained from *ab initio* calculations at room temperature using the BoltzTraP software package. For the measured Seebeck coefficient, there are two possibilities for corresponding carrier concentrations, as shown by solid and open symbols in Fig. 4(f). Using the electrical conductivity data and those from the DFT calculations shown in Fig. 4(g), the solid symbols were considered to estimate carrier concentrations for the samples as the values obtained in the intrinsic regime (open symbols) are very far from the measured electrical conductivities. The lower electrical conductivity of the p-type PbS–S–SPS sample can be due to its lower carrier concentration ($p = 1.8 \times 10^{18}$ cm^{-3}) compared to that of the n-type PbS-SPS with a higher carrier concentration ($n = 3.7 \times 10^{19}$ cm^{-3}) [Fig. 4(g)], as well as its higher concentration of grain boundaries. The measured values for both n-type and p-type cases were much lower than those predicted by DFT calculations, which is expected as the DFT model represents a single crystalline material with no grain boundary-induced energy barrier as opposed to our polycrystalline samples. Thus, we can view the DFT-predicted conductivities as upper values to the electrical conductivity at each carrier concentration. For the p-type sample, the calculated electrical conductivity and the measured electrical conductivity were $\sigma_{DFT} = 27.7$ S · cm^{-1} and $\sigma_{exp} = 6.1$ S · cm^{-1}, respectively. For the n-type sample, the calculated electrical conductivity and the measured electrical conductivity were $\sigma_{DFT} = 509.1$ S · cm^{-1}

and σ_{exp} = 20.6 S · cm^{-1}, respectively. It can be seen that the electrical conductivity of the *p*-type sample was actually much closer to the predicted single crystalline value (22% of σ_{DFT}) at its carrier concentration than that of the n-type sample (4% of σ_{DFT}).

Using Seto's formulations,[26] the barrier height for charge carriers during transport vs carrier concentration is plotted in Fig. 4(h) for each sample. The lower limits of carrier concentration were estimated from experimental Seebeck measurements and DFT calculations, and the upper limits were based on the performed ICP-OES analysis. Based on Seto's formulations, in the range $NL > Q_t$, the height of the barrier decreases as the carrier concentrations increase ($E_B \propto 1/N$). For the PbS-SPS (x = 0.19), PbS–S–SPS (x = −0.03), and PbS-ref.–SPS (x = 0.04), the density of trap states and barrier heights of $Q_t = 2.04 \times 10^{14}$, 2.92×10^{13}, and 6.12×10^{13} cm^{-2} and E_B = 0.352, 0.046, and 0.151 eV were calculated, respectively [see Table I and Fig. 4(g)]. For PbS-ref.–SPS sample, the barrier height was calculated only in temperatures above 600 K in the linear region of the logarithmic curve shown in Fig. 4(c). Because the grain boundaries and morphologies of the PbS-SPS and PbS–S–SPS seemed to be similar using TEM and SEM analysis, the much higher barrier height of the former compared to the latter (sulfurized sample with no $V_{\ddot{S}}$) is attributed to the high concentration $V_{\ddot{S}}$ vacancies. Each $V_{\ddot{S}}$ can introduce two negative charges which can essentially be trapped in the interfaces creating a highly charged barrier against the charge transport. The different temperature-dependent electrical conductivity of the reference sample compared to solvothermally synthesized samples can be due to its much lower grain boundary density (through lower surface area and higher particle size), as shown in Fig. S2 in the supplementary material.

Temperature-dependent total thermal conductivity and lattice thermal conductivity of the samples are shown in Figs. 5(a) and 5(b). The expression $\kappa_L = \kappa - \sigma LT$ can be used to extract the lattice thermal conductivity from the total thermal conductivity, where L is the Lorenz number and is a function of chemical potential. The Lorenz numbers were calculated based on the measured Seebeck coefficients according to Kim *et al.*[35] assuming single band transport (Fig. S3, supplementary material). PbS-SPS and PbS–S–SPS exhibited lower lattice thermal conductivities compared to those of PbS-ref.–SPS although all samples displayed anharmonic phonon-phonon dominated transport, indicating that thermal transport was not influenced as strongly by the grain boundaries in this regime, which can be the case for transport across even weaker van der Waals interfaces at room temperature.[36] The porosity-corrected thermal conductivity of PbS-ref.–SPS decreased more rapidly as the temperature increased approaching those of the other samples. Porosity corrected values of 1.081, 1.28, and 1.23 W m^{-1} K^{-1} was measured

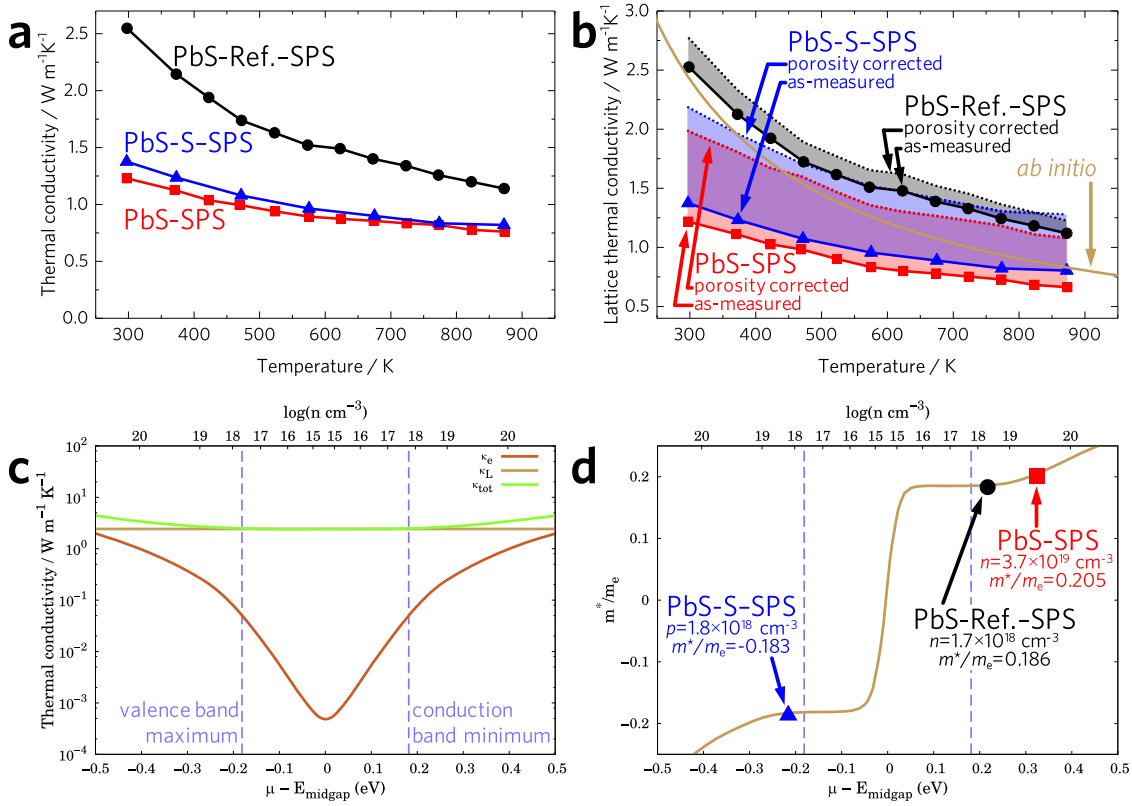

FIG. 5. (a) Measured temperature-dependent total thermal conductivity values of the PbS samples. (b) Lattice thermal conductivity of the samples without (symbols, solid lines) and with (dotted lines) porosity corrections; the Lorenz number has been obtained according to Ref. 35. (c) DFT calculated electronic, lattice, and total thermal conductivity of PbS at 300 K. (d) DFT calculated effective mass for PbS at 300 K.

for PbS-SPS and PbS–S–SPS and PbS-ref.–SPS, at a temperature of 600 °C, respectively. The porosity correction calculation was based on the measured density compared to that of the theoretical value according to the Eucken[37,38] and Russell[39] models. DFT calculations estimated the lattice thermal conductivity to be 0.833 W m^{-1} K^{-1} at ~600 °C. The DFT calculated total thermal conductivity and lattice and electronic contributions are shown in Fig. 5(c). The calculated effective mass values are demonstrated in Fig. 5(d). Additionally, prior to thermal diffusivity measurements using a NETZSCH LFA-457 Microflash, pyrex 7740 and pyroceram 9606 reference samples were measured and the obtained data were compared with that provided from NETZSCH Group. An excellent agreement was observed as shown in Fig. S4 of the supplementary material.

Multiple runs of the electrical conductivity, Seebeck coefficient, and thermal conductivity measurements have been conducted (Fig. S5, supplementary material). First, thermal diffusivity measurements were conducted on the pellets obtained from SPS at 600 and 700 °C. Good agreement between the first and the second run of thermal conductivity measurements for the pellet obtained by SPS at 600 °C is shown in Fig. S5(a) of the supplementary material after conversion to thermal conductivity. Good reproducibility is also observed between the heating and cooling thermal conductivity curves of the sample obtained by SPS at 700 °C, as illustrated in Fig. S5(b), supplementary material. After the thermal diffusivity measurements, the samples were cut into rectangular bars, and the surfaces were repolished for the electrical conductivity and Seebeck coefficient measurements using a ZEM-3 instrument. Figure S5(c) of the supplementary material compares the 1st and 2nd electrical measurement runs for a bar obtained from a pellet with SPS at 600 °C. Interestingly, in the second run, the sample exhibited higher values of electrical conductivity at temperatures below ~525 °C (e.g., 44.5 S cm^{-1} compared to 14.9 S cm^{-1} at room temperature for the 2nd and 1st runs, respectively). However, the electrical conductivity values for both runs approached 71.3 S cm^{-1} at higher temperatures. This behavior can be explained by using the barrier height vs carrier concentration plot shown in Fig. 4(h). After each run at the temperature range up to 600 °C, the carrier concentration increases due to further sulfur evaporation. This increases the carrier concentration, and therefore, the barrier height decreases leading to the enhancement in electrical conductivity. Furthermore, in the high temperature regime, the charge carriers have gained enough thermal energy to overcome the barrier causing the electrical conductivities to approach the same value. Seebeck coefficients remain relatively close within the range of the measurement uncertainty despite expected sulfur evaporation [Fig. S5(d), supplementary material]. This can be explained since the carrier concentration is in the degenerate regime where the change in the Seebeck coefficient with carrier concentration remains fairly small. By contrast, the barrier height changes rapidly vs the carrier concentration (based on $E_B \propto 1/N$). A similar trend was seen between the first and second run of the sample made from a pellet with SPS at a higher temperature of 700 °C [Figs. S5(e) and S5(f), supplementary material]. During the first run, the electrical conductivity decreased as the temperature increased from 302 to 417 K. However, as the temperature was further raised above 466 K, the electrical conductivity started to increase with temperature. For this first measurement, transport appeared to be governed by electron-phonon scattering at lower temperatures, whereas at the higher temperatures (above 466 K), it was more affected by the grain boundary energy barrier. This can arise due to the more effective sintering of the grain boundaries in this sample as the SPS was conducted at the higher temperature of 700 °C. As the SPS temperature increases, the grain sintering is improved and the effects of the grain boundary energy barrier start to diminish. The better sintering is supported by the measured mass density of this sample (6.65 g cm^{-1}) which was higher than that of the sample with SPS at 600 °C (6.28 g cm^{-1}) but still lower than that of the reference sample (7.34 g cm^{-1}). Interestingly, the 2nd run of this sample exhibited an electrical conductivity trend completely dominated by the electron-phonon scattering similar to the trend of the reference sample and single crystals with no grain boundaries. Both, the first and second measurement runs approached the same limit above 756 K.

A good agreement between the first and second run thermal conductivity measurements of the reference sample obtained by SPS at 600 °C is shown in Fig. S6(a) of the supplementary material. The electrical conductivity and Seebeck coefficient measurements of two rectangular bars from the same pellet have been shown in Figs. S6(b) and S6(c) of the supplementary material, indicating that the sintered pellet is homogeneous. A figure of merit for the PbS samples is shown in Fig. S7 of the supplementary material.

In conclusion, the effects of highly charged interfaces on the electrothermal transport properties of PbS_{1-x} were investigated in detail. Dendritic PbS_{1-x} samples with $x = 0.19$ and -0.03 and a reference sample with $x = 0.04$ were investigated in order to understand the effects of interfaces on transport properties. High concentrations of grain boundaries were observed for the samples synthesized using a solvothermal method with dendritic structures compared to the cubic morphology reference sample. Sulfur vacancies were formed during the annealing process with a major mass loss occurring at 266 °C. DFT calculations suggested that this loss could be attributed to the regions close to the particle surfaces as the $V_{\ddot{S}}$ formation energy on the surface was 1.72 times lower than that through the bulk. A postsynthesis thermal sulfurization process prevented $V_{\ddot{S}}$ vacancy formation, resulting in *p*-type samples. The electrical conductivity behavior of the substoichiometric PbS-SPS ($x = 0.19$) and PbS–S–SPS ($x = -0.03$) samples was dominated by thermionic transport through charged interface barriers, whereas the electrical conductivity behavior of PbS-ref.–SPS ($x = 0.04$) was dominated by electron-phonon scattering at temperatures below ~325 °C due to lower concentration of grain boundaries. Barrier heights for charge carriers during electrothermal transport of $E_B = 0.352$, 0.151, and 0.046 eV were estimated for PbS-SPS, PbS–S–SPS, and PbS-ref.–SPS. The much larger barrier height occurring in PbS-SPS was found to arise from a high density of $V_{\ddot{S}}$ defects charging the interfaces and thus raising the barrier potential. This investigation has described $V_{\ddot{S}}$ site formation and revealed the crucial role of interfaces and interface-vacancy interactions in dominating the electrothermal transport properties of substoichiometric PbS.

See supplementary material for details of theoretical and experimental methods; XRD analysis of the samples obtained by SPS; calculated Lorenz number based on the measured Seebeck coefficient; thermal conductivity of reference samples pyrex 7740 and pyroceram 9606; thermal conductivity, electrical conductivity, and Seebeck coefficient measurements of the samples obtained by SPS at 600 and 700 °C; and 1st and 2nd run thermal conductivity measurements of

the reference sample, electrical conductivity, and Seebeck coefficient measurements of the reference samples conducted on two different rectangular bars from the same pellet.

This project was conceived and led by M.T.P. and S.Y. Experimental work and materials synthesis by M.T.P., S.Y., R.K.-S., and R.D.M. were supported by the U. S. National Science Foundation Award Nos. CAREER-1553987 (M.T.P., S.Y., and R.K.-S.) and REU-1560098 (M.T.P. and R.D.M.), the UConn Research Foundation, Award No. PD17-0137 (M.T.P., S.Y., and R.K.-S.), the U.S. Department of Energy Office of Science under Contract No. 89233218CNA000001 (M.T.P.), and a GE Graduate Fellowship for Innovation (S.Y.); theoretical and computational work was conducted by T.D.H. and supported by XSEDE through the computational resource allocation Grant No. TG-DMR170031.

REFERENCES

[1] Z.-H. Ge, L.-D. Zhao, D. Wu, X. Liu, B.-P. Zhang, J.-F. Li, and J. He, "Low-cost, abundant binary sulfides as promising thermoelectric materials," Mater. Today **19**, 227 (2016).
[2] S. R. Taylor, "Abundance of chemical elements in the continental crust: A new table," Geochim. Cosmochim. Acta **28**, 1273 (1964).
[3] L.-D. Zhao, J. He, S. Hao, C.-I. Wu, T. P. Hogan, C. Wolverton, V. P. Dravid, and M. G. Kanatzidis, "Raising the thermoelectric performance of p-type PbS with endotaxial nanostructuring and valence-band offset engineering using CdS and ZnS," J. Am. Chem. Soc. **134**, 16327 (2012).
[4] W. W. Scanlon, "Recent advances in the optical and electronic properties of PbS, PbSe, PbTe and their alloys," J. Phys. Chem. Solids **8**, 423 (1959).
[5] G. D. Mahan, "Figure of merit for thermoelectrics," J. Appl. Phys. **65**, 1578 (1989).
[6] S. Yazdani and M. T. Pettes, "Nanoscale self-assembly of thermoelectric materials: A review of chemistry-based approaches," Nanotechnology **29**, 432001 (2018).
[7] S. Johnsen, J. He, J. Androulakis, V. P. Dravid, I. Todorov, D. Y. Chung, and M. G. Kanatzidis, "Nanostructures boost the thermoelectric performance of PbS," J. Am. Chem. Soc. **133**, 3460 (2011).
[8] L.-D. Zhao, S.-H. Lo, J. He, H. Li, K. Biswas, J. Androulakis, C.-I. Wu, T. P. Hogan, D.-Y. Chung, V. P. Dravid, and M. G. Kanatzidis, "High performance thermoelectrics from earth-abundant materials: Enhanced figure of merit in PbS by second phase nanostructures," J. Am. Chem. Soc. **133**, 20476 (2011).
[9] A. A. El-Sharkawy, A. M. Abou El-Azm, M. I. Kenawy, A. S. Hillal, and H. M. Abu-Basha, "Thermophysical properties of polycrystalline PbS, PbSe, and PbTe in the temperature range 300-700 K," Int. J. Thermophys. **4**, 261 (1983).
[10] H. Wang, J. Wang, X. Cao, and G. J. Snyder, "Thermoelectric alloys between PbSe and PbS with effective thermal conductivity reduction and high figure of merit," J. Mater. Chem. A **2**, 3169 (2014).
[11] L.-D. Zhao, J. He, C.-I. Wu, T. P. Hogan, X. Zhou, C. Uher, V. P. Dravid, and M. G. Kanatzidis, "Thermoelectrics with earth abundant elements: High performance *p*-type PbS nanostructured with SrS and CaS," J. Am. Chem. Soc. **134**, 7902 (2012).
[12] M. Ibáñez, Z. Luo, A. Genç, L. Piveteau, S. Ortega, D. Cadavid, O. Dobrozhan, Y. Liu, M. Nachtegaal, M. Zebarjadi, J. Arbiol, M. V. Kovalenko, and A. Cabot, "High-performance thermoelectric nanocomposites from nanocrystal building blocks," Nat. Commun. **7**, 10766 (2016).
[13] M. Ibáñez, R. Zamani, S. Gorsse, J. Fan, S. Ortega, D. Cadavid, J. R. Morante, J. Arbiol, and A. Cabot, "Core–shell nanoparticles as building blocks for the bottom-up production of functional nanocomposites: PbTe–PbS thermoelectric properties," ACS Nano **7**, 2573 (2013).
[14] R. Guo, X. Wang, Y. Kuang, and B. Huang, "First-principles study of anisotropic thermoelectric transport properties of IV-VI semiconductor compounds SnSe and SnS," Phys. Rev. B **92**, 115202 (2015).
[15] Z. Tian, J. Garg, K. Esfarjani, T. Shiga, J. Shiomi, and G. Chen, "Phonon conduction in PbSe, PbTe, and $PbTe_{1-x}Se_x$ from first-principles calculations," Phys. Rev. B **85**, 184303 (2012).
[16] Z. Tian, S. Lee, and G. Chen, "Heat transfer in thermoelectric materials and devices," ASME J. Heat Transfer **135**, 061605 (2013).
[17] G. H. Carey, A. L. Abdelhady, Z. Ning, S. M. Thon, O. M. Bakr, and E. H. Sargent, "Colloidal quantum dot solar cells," Chem. Rev. **115**, 12732 (2015).
[18] S. K. Bux, J.-P. Fleurial, and R. B. Kaner, "Nanostructured materials for thermoelectric applications," Chem. Commun. **46**, 8311 (2010).
[19] M. Ibáñez, R. J. Korkosz, Z. Luo, P. Riba, D. Cadavid, S. Ortega, A. Cabot, and M. G. Kanatzidis, "Electron doping in bottom-up engineered thermoelectric nanomaterials through HCl-mediated ligand displacement," J. Am. Chem. Soc. **137**, 4046 (2015).
[20] R. J. Mehta, Y. Zhang, C. Karthik, B. Singh, R. W. Siegel, T. Borca-Tasciuc, and G. Ramanath, "A new class of doped nanobulk high-figure-of-merit thermoelectrics by scalable bottom-up assembly," Nat. Mater. **11**, 233 (2012).
[21] J. Li, Q. Tan, and J.-F. Li, "Synthesis and property evaluation of $CuFeS_{2-x}$ as earth-abundant and environmentally-friendly thermoelectric materials," J. Alloys Compd. **551**, 143 (2013).
[22] W. W. Scanlon, "Interpretation of Hall effect and resistivity data in PbS and similar binary compound semiconductors," Phys. Rev. **92**, 1573 (1953).
[23] M. T. Pettes, J. Kim, W. Wu, K. C. Bustillo, and L. Shi, "Thermoelectric transport in surface- and antimony-doped bismuth telluride nanoplates," APL Mater. **4**, 104810 (2016).
[24] J. Horák, P. Lošťák, L. Koudelka, and R. Novotný, "Inversion of conductivity type in $Bi_2Te_{3-x}S_x$ crystals," Solid State Commun. **55**, 1031 (1985).
[25] H. Wu, J. Carrete, Z. Zhang, Y. Qu, X. Shen, Z. Wang, L.-D. Zhao, and J. He, "Strong enhancement of phonon scattering through nanoscale grains in lead sulfide thermoelectrics," NPG Asia Mater. **6**, e108 (2014).
[26] J. Y. W. Seto, "The electrical properties of polycrystalline silicon films," J. Appl. Phys. **46**, 5247 (1975).
[27] P. Rai-Choudhury and P. L. Hower, "Growth and characterization of polycrystalline silicon," J. Electrochem. Soc. **120**, 1761 (1973).
[28] T. I. Kamins, "Hall mobility in chemically deposited polycrystalline silicon," J. Appl. Phys. **42**, 4357 (1971).
[29] M. Scheele, N. Oeschler, I. Veremchuk, S.-O. Peters, A. Littig, A. Kornowski, C. Klinke, and H. Weller, "Thermoelectric properties of lead chalcogenide core–shell nanostructures," ACS Nano **5**, 8541 (2011).
[30] K. Kushnir, K. Chen, L. Zhou, B. Giri, R. L. Grimm, P. M. Rao, and L. V. Titova, "Dynamics of photoexcited carriers in polycrystalline PbS and at PbS/ZnO heterojunctions: Influence of grain boundaries and interfaces," J. Phys. Chem. C **122**, 11682 (2018).
[31] J. Martin, L. Wang, L. Chen, and G. S. Nolas, "Enhanced Seebeck coefficient through energy-barrier scattering in PbTe nanocomposites," Phys. Rev. B **79**, 115311 (2009).
[32] A. Popescu, L. M. Woods, J. Martin, and G. S. Nolas, "Model of transport properties of thermoelectric nanocomposite materials," Phys. Rev. B **79**, 205302 (2009).
[33] T. K. Gupta, "Application of zinc oxide varistors," J. Am. Ceram. Soc. **73**, 1817 (1990).
[34] S. Yazdani, R. Kashfi-Sadabad, T. D. Huan, M. D. Morales-Acosta, and M. T. Pettes, "Polyelectrolyte-assisted oxygen vacancies: A new route to defect engineering in molybdenum oxide," Langmuir **34**, 6296 (2018).
[35] H.-S. Kim, Z. M. Gibbs, Y. Tang, H. Wang, and G. J. Snyder, "Characterization of Lorenz number with Seebeck coefficient measurement," APL Mater. **3**, 041506 (2015).
[36] M. T. Pettes and L. Shi, "A reexamination of phonon transport through a nanoscale point contact in vacuum," ASME J. Heat Transfer **136**, 032401 (2014).
[37] A. Eucken, Ceram. Abstr. **11**, 576 (1932).
[38] A. Eucken, Ceram. Abstr. **12**, 231 (1933).
[39] H. W. Russell, "Principles of heat flow in porous insulators," J. Am. Ceram. Soc. **18**, 1 (1935).